aerospace

MDPI

Article

Effect of Characteristic Phenomena and Temperature on Super-Cooled Large Droplet Icing on NACA0012 Airfoil and Axial Fan Blade

Toma Takahashi [1,†], Koji Fukudome [1,*,†], Hiroya Mamori [2,†], Naoya Fukushima [3], and Makoto Yamamoto [1,†]

1 Department of Mechanical Engineering, Tokyo University of Science, 6-3-1 Niijuku, Katsushika-ku, Tokyo 125-8585, Japan; 4518533@alumni.tus.ac.jp (T.T.); yamamoto@rs.tus.ac.jp (M.Y.)
2 Department of Mechanical and Intelligent Systems Engineering, The University of Electro-Communications, 1-5-1, Chofugaoka, Chofu, Tokyo 182-8585 Japan; mamori@uec.ac.jp
3 Department of Prime Mover Engineering, Tokai University, 4-1-1 Kitakaname, Hiratsuka-shi, Kanagawa 259-1292, Japan; fukushima@tsc.u-tokai.ac.jp
* Correspondence: kfukudome@rs.tus.ac.jp; Tel.: +81-3-5876-1333
† These authors contributed equally to this work.

Received: 10 June 2020; Accepted: 30 June 2020; Published: 3 July 2020



Abstract: Icing simulations involving super-cooled large droplets (SLDs) on a NACA0012 airfoil and a commercial axial fan were performed considering the characteristic behavior of SLD icing (i.e., splash-bounce, deformation, and breakup). The simulations were performed considering weak coupling between flow field and droplet motion. The flow field was computed using the Eulerian method, wherein the droplet motion was simulated via the Lagrangian method. To represent the ice shape, an extended Messinger model was used for thermodynamic computation. The ice shape and collection efficiency of the NACA0012 airfoil derived using the icing simulation exhibited a reasonable agreement with the existing experimental data. The icing simulation results for the axial fan, in terms of distribution of ice on the blade and its influence on the flow field, indicated that flow separation occurred, and the mass flow rate of the flow passage decreased. Moreover, the splash and bounce phenomena considerably influenced the icing process; however, the effect of the deformation and breakup phenomena was negligibly small. In terms of the effect of the SLDs on the icing phenomena, it was noted that, with the decrease in the SLD temperature (from −5 °C to −15 °C), the number of adhering SLDs increased, whereas the number of splashing and bouncing SLDs decreased.

Keywords: icing simulation; super-cooled droplet; large droplet; NACA0012 airfoil; numerical simulation

1. Introduction

The icing phenomenon, which commonly occurs in aircraft and involves super-cooled droplets impinging and accreting on a solid surface, has been recognized as a critical safety problem. In particular, icing induced in pitot tubes may lead to an incorrect indication. The accreted ice on a wall surface increases the surface roughness, thereby increasing the skin friction and pressure drag, which may reduce the aerodynamic and engine performance. Moreover, in jet engines, ice shedding from blades and vanes may cause critical damage and engine failure. To address these issues pertaining to in-flight icing, several numerical and experimental studies have been performed.

With recent advancements in computational abilities, numerical simulations represent a powerful tool to investigate the icing phenomenon. However, performing icing simulations is challenging as the icing is often a result of super-cooled droplets and corresponds to a multi-physics phenomenon. Nevertheless, several models are available to simulate the icing process. Zhang et al. [1] developed

an icing model to describe the aircraft icing process based on a solid–liquid phase-change theory. This model involves wet and dry modes, which can be switched depending on the icing condition. Fortin et al. [2] developed a surface roughness model of ice to evaluate the retention, runback, and shedding of liquid water on an airfoil surface. Recently, a computational model of "mixed ice" incorporating both rime and glaze ices was also developed [3]. Rime ice refers to a super-cooled droplet that impinges on the wing and freezes instantaneously, and glaze ice refers to the water film created by an impinged droplet running back along the wing and freezing. The former and latter phenomena occur at low (less than −15 °C) and relatively higher temperature (more than −10 °C) conditions, respectively.

Furthermore, three-dimensional icing simulations for a wing and airfoil have been performed using icing models. To examine the effect of icing on the lift and drag forces, some researchers performed icing simulations for a swept wing under rime and glaze ice accretion conditions [4] and for an unmanned aerial vehicle [5]. Shen et al. [6] performed a three-dimensional numerical simulation to reproduce the ice accretion on the engine inlet. Wang and Zhu [7] investigated the influence of centrifugal forces on three-dimensional rotor blade icing and reported that the centrifugal force affects the flow direction and distribution of the liquid water on the surfaces. In addition, icing simulation platforms have been developed. NASA developed the icing simulation code named "LEWICE", which is widely used. For example, Narducci [8] used this code to perform an icing simulation for the rotor blades of a helicopter flying through an icing cloud. Moreover, the Italian aerospace research center (CIRA: Centro Italiano Ricerche Aerospaziali) developed an icing simulation code that is used to evaluate the icing on single and multielement airfoils [9].

Most existing research has focused on super-cooled droplets with a diameter of less than 20 μm because aircraft usually cruise at altitudes involving many "small" super-cooled droplets. These droplets are assumed to adhere on the solid surface without bouncing and retain their spherical shape owing to the surface tension. The icing model for such small droplets has been established to predict and simulate the icing phenomenon.

However, in 1994, an aircraft crashed owing to icing incurred by super-cooled large droplets (SLDs). SLDs refer to droplets with a diameter larger than 40 μm, and they exhibit the following characteristic events:

- splashing, wherein the impinged droplets separate into adhering and rebounding masses;
- bouncing, wherein the entire mass of the impinged droplet rebounds;
- deformation, in which a flying droplet deforms into a disk due to the shear force acting on the droplet;
- breakup, wherein flying droplet breaks up and generates secondary droplets.

These phenomena do not occur in the case of super-cooled small droplets. As SLD icing is a critical problem in aircraft and threatens flight safety, numerical models to represent its characteristic events have been established. Wright and Potapczuk [10] used the LEWICE code to perform icing simulations on an airfoil, considering the splashing of SLDs. They reported that the collection efficiency is considerably degraded in the event of splashing, whose degree depends on the droplet size and impinging velocity, and that the Weber number is a key parameter in the icing process. Zhang and Liu [11] experimentally investigated the effect of the droplet size on the thermodynamics pertaining to the SLD impingement and reported that the droplet size considerably influences the heat transfer between the film–substrate interfaces; this aspect was verified by a theoretical analysis. In addition, they developed an impinging heating model and applied it to the SLD icing simulation. Wang et al. [12] developed a splashing model for the SLD impingement and performed icing simulations for clean and iced NACA23012 airfoils, based on the Lagrangian approach. The droplet splashing ratio and splashing mass loss ratio on the surface have also been computed [13]. To reduce the computational cost pertaining to the Lagrangian approach, SLD simulations based on the Eulerian approach have been performed. Honsek et al. [14] proposed a model for the impinging droplet behavior including splashing and bouncing phenomena, represented as a body force in the

governing equation. Bilodeau et al. [15] extended Honsek et al.'s model to examine the effect of the postimpact droplets and performed an icing simulation for clean and iced NACA23012 and MS(1)-0317 airfoils. In addition, SLD icing consisting of droplet deformation and wall interaction as splash simulated using a commercial solver [16]. Recent developments in numerical simulations on SLD icing are well summarized in a previous review [17].

As discussed, several numerical models considering the splash and bounce phenomena for SLD icing have been developed. However, the influence of the deformation and breakup of SLDs has not been clarified. The deformation of SLDs likely changes the drag coefficient, which affects the droplet trajectory, and the breakup of the droplet decreases the droplet size, which affects the impingement behavior (i.e., splash and bounce) of SLDs. To examine these aspects, in this study, SLD icing simulations for a NACA0012 airfoil and a commercial axial fan blade were performed considering the characteristic behavior of SLDs, i.e., splash, bounce, deformation, and breakup. In the icing simulation for the airfoil, the influence of each event on the ice shape was examined, and the resulting ice shape was compared with the experimental data. In the icing simulation for the fan blade, the variation in the flow field and mass flow rate owing to the icing and the influence of the SLD events and SLD temperature on the ice shape were investigated.

2. Numerical Procedure

In general, the time scale of the flow field around the wing and fan is considerably different from that of the ice accretion and growth; therefore, in the performed simulation, these aspects were weakly coupled. The numerical procedure involved the following five steps:

1. generate the computational grids;
2. compute the flow field;
3. compute the droplet trajectory to determine the distribution of the impinged droplet on the surface of the wing and blade;
4. compute the thermodynamics to obtain the ice shape;
5. regenerate the computational grids to fit the ice shape, and repeat steps 2–5.

These steps are explained in detail in the following text.

2.1. Computational Grids

The computational grid for the flow around the wing and blade was established using an overset grid system involving two computational grids: the main grid, whose resolution is coarser than the sub grid and is used to obtain the global flow field; and the sub grid, with a fine resolution, used to obtain the precise flow field around the wing and blade. The present grid resolution has been validated in our previous study [18], indicating that it provides reasonable results practically.

2.2. Flow Field

The flow field around the wing and blade was computed using the Eulerian manner. The governing equations were the continuity, Navier–Stokes, and energy equations for three-dimensional, compressible, and turbulent flows. The second-order upwind total variation diminishing scheme [19] and the second-order central differential scheme were used for the inviscid and viscous terms, respectively. The lower-upper alternating direction implicit (LU-ADI) scheme [20] was used for the time integration. The Kato–Launder k-ε model [21] was used as the turbulent model because it can avoid excessive generation of turbulent eddy viscosity around the leading edge.

2.3. Droplet Trajectory

An one-way coupling method was employed because we supposed that the volumetric fraction of the droplets to the air is sufficiently low. The droplet trajectory was computed in the Lagrangian

manner: the droplets do not affect the flow field; however, the flow field affects the droplet motion. The forces acting on the droplets are drag, centrifugal, and Coriolis forces, and the motion equation of the droplet is as follows:

$$\frac{\mathrm{d}^2\boldsymbol{U}_d}{\mathrm{d}t^2} = \frac{3}{4}C_D\frac{1}{d_d}\frac{\rho_f}{\rho_d}\boldsymbol{U}_r\left|\boldsymbol{U}_r\right| - \left(2\boldsymbol{\Omega}\times\boldsymbol{U}_d - \boldsymbol{\Omega}\times\left(\boldsymbol{\Omega}\times\boldsymbol{r}_d\right)\right), \tag{1}$$

where $\boldsymbol{r}$, $\boldsymbol{U}$, and $\boldsymbol{\Omega}$ represent the position, velocity, and angular velocity vectors of the rotating reference, respectively. The subscripts f and d denote the flow field and droplet, respectively, and $\boldsymbol{U}_r$ is the relative velocity between the flow field and the droplet, where $\boldsymbol{U}_r = \boldsymbol{U}_d - \boldsymbol{U}_f$. In addition, t, ρ, d_d, and C_D denote the time, density, diameter, and drag coefficient, respectively. Based on the results of the droplet trajectory, the collection efficiency (E_{col}), which is the number of adhered droplets per unit area, on the wing and blade was determined.

2.4. Icing Model

This section describes the models for the deformation, breakup, and splash-bounce characteristic phenomena in the SLD icing simulation. Deformation and breakup occur when a droplet is flying in the flow field, whereas the splash-bounce phenomenon occurs when a droplet collides on the wall.

In this study, the deformation model proposed by Clift [22] was employed. The deformation of the droplet affects the drag coefficients C_D in Equation (1), corresponding to the drag from the flow field. In this model, C_D is the sum of the drag coefficient of the disk and the sphere, $C_{D,Disk}$ and $C_{D,Sphere}$, respectively, as

$$C_D = eC_{D,Disk} + (1-e)\,C_{D,Sphere}. \tag{2}$$

$C_{D,Disk}$ and $C_{D,Sphere}$ are computed as

$$C_{D,Disk} = 1.1 + \frac{64}{\pi \mathrm{Re}_{d\,r}}, \tag{3}$$

$$C_{D,Sphere} = \frac{24}{\mathrm{Re}_{d\,r}}\left(1 + 0.15\mathrm{Re}_{d\,r}^{0.687}\right), \tag{4}$$

where the droplet Reynolds number and viscosity μ_d are defined as

$$\mathrm{Re}_{d\,r} = \frac{d_d U_r \rho_d}{\mu_d}, \tag{5}$$

$$\mu_d(T) = 0.5936\exp\left(-0.07959T + 1.131\exp\left(-0.006327T\right)\right)\times 10^{-3}. \tag{6}$$

The viscosity μ_d [Pa] (and the surface tension, as discussed later) is calculated using an empirical formula [23], and it is a function of the droplet temperature T [°C]. e in Equation (2) is a weight function based on the Weber number $\mathrm{We} = d_d U_r^2 \rho_d / \sigma_d$ as

$$e = 1 - \frac{1}{\left(1 + 0.007\sqrt{\mathrm{We}}\right)^6}, \tag{7}$$

where the surface tension σ_d [N/m] can be defined as

$$\sigma_d(T) = (-0.158T + 75.08)\times 10^{-3}. \tag{8}$$

Accordingly, the influence of the deformation on the drag coefficient is characterized by the Weber number: When We is large, the C_D of the SLD droplet approaches that of the disk; when We is small, C_D approaches that of the sphere.

When the SLD is flying, it breaks up and loses mass owing to the instability of the surface tension. The breakup model by Hsiang and Faeth [24] represents this loss as a variation of the diameter of the SLD, d_d. The SLD is assumed to be spherical, except when estimating the drag. The breakup occurs when We is larger than 13, and d_d varies as

$$d_d = 6.2 d_{d,before} \left(\frac{\rho_d}{\rho_f} \right)^{1/4} \mathrm{Re}_{dr}^{-1/2}, \tag{9}$$

where $d_{d,before}$ is the diameter of the droplet before breaking up. The broken SLD does not exhibit any change in the flying direction and velocity magnitude.

If the SLD approaches the wall at a distance less than the radius, it is treated as an impinging SLD. The impinging SLD begins to freeze when it touches the wall surface. As the SLD is larger than an ordinary super-cooled droplet, it exhibits three types of impinging behavior: the complete mass of the droplet adheres; some of the mass of the droplet adheres on the wall surface, whereas the other mass is dispersed owing the splash and bounce phenomena; and the SLD rebounds perfectly. In the splash-bounce model developed by Wright et al. [25,26], a splashing parameter K_L and ratio of the droplet diameter before and after icing d_{after}/d are used to determine the droplet behavior:

$$K_L = \frac{0.859 \sqrt{\mathrm{Oh}_d \mathrm{Re}_{dn}^{5/4}} \left(\frac{\rho_d}{LWC} \right)^{1/8}}{\sin \alpha}, \tag{10}$$

$$\frac{d_{after}}{d} = 8.72 \exp \left(-0.0281 \mathrm{Oh}_d \mathrm{Re}_{dn}^{5/4} \right). \tag{11}$$

Here, α and LWC denote the angle of attack against the surface and liquid water content, respectively. The droplet Reynolds number Re_{dn} is defined as

$$\mathrm{Re}_{dn} = \frac{\rho_d V_n d_d}{\mu_d}, \tag{12}$$

where the characteristic velocity V_n is the wall normal velocity, which is different from the velocity pertaining to Re_{dr}. The droplet Ohnesorge number Oh_d is defined as

$$\mathrm{Oh}_d = \frac{\mu_d}{(\rho_d \sigma_d d_d)^{1/2}}. \tag{13}$$

For $K_L \leqq 200$, the droplet adheres. For $K_L > 200$, three different events occur: At $d_{after}/d \geqq 1$, the droplet adheres; at $0.05 < d_{after}/d < 1$, the droplet splashes; at $d_{after}/d \leqq 0.05$, the droplet bounces. The mass of the droplet before splash and the loss of the mass caused by the splash are denoted as m and m_{loss}, respectively, and defined as follows:

$$\frac{m_{loss}}{m} = 0.7(1 - \sin \alpha) \left\{ 1 - \exp(K_L - 200) \right\}. \tag{14}$$

The tangential velocity V_t and wall-normal velocity V_n of the droplet before and after splashing are described by follows:

$$\frac{V_{t,after}}{V_t} = 1.075 - 0.0025\alpha, \tag{15}$$

$$\frac{V_{n,after}}{V_n} = 0.3 - 0.002\alpha. \tag{16}$$

The subscripts t and n denote the tangential and normal directions, respectively.

2.5. Thermodynamics

The thermodynamics of ice generation and growth are computed using the extended Messinger model [27], which is based on the Stefan problem (i.e., a standard method for phase-change problems). This model can be used to evaluate the smooth transition from the rime ice to glaze ice. The governing equations for the extended Messinger model are

$$\frac{\partial T_i}{\partial t} = \frac{k_i}{\rho_i C_{pi}} \frac{\partial^2 T_i}{\partial y_{iw}^2}, \tag{17}$$

$$\frac{\partial T_w}{\partial t} = \frac{k_w}{\rho_w C_{pw}} \frac{\partial^2 T_w}{\partial y_{iw}^2}, \tag{18}$$

$$\rho_i \frac{\partial B_i}{\partial t} + \rho_w \frac{\partial B_w}{\partial t} = m_{im} + m_{in} - m_{e,s}, \tag{19}$$

$$\rho_i L_F \frac{\partial B_i}{\partial t} = k_i \frac{\partial T}{\partial y_{iw}} - k_w \frac{\partial T_w}{\partial y_{iw}}. \tag{20}$$

Here, T, k, C_p, B, and y_{iw} denote the density, temperature, thermal conductivity, specific heat, thickness, and distance from the wall, respectively. The subscripts i and w represent ice and water, respectively.

These equations are applied for each grid, and ice is assumed to be generated perpendicular to the airfoil surface. Equations (17) and (18) are the equations of heat conduction for the ice and water layers, respectively; Equation (19) is the mass conservation equation (m_{im}, m_{in}, and $m_{e,s}$ denote the impinged, runback, and evaporation (or sublimation) mass flux, respectively); and Equation (20) represents the phase-change condition at the interface between the ice and water (LF in Equation (20) denotes the latent heat by the condensation of water). These equations are spatially discretized using the second-order central differential scheme, and the fourth-order Runge–Kutta method is employed for the time integration.

3. Validation of Icing Simulation Method for NACA Airfoil

The two-dimensional SLD icing simulation of the NACA0012 airfoil was performed to validate the present simulation. Figure 1 shows the computational domain and grids. A C-type computational domain sized $10c \times 10c$ was used, as shown in Figure 1a. The total temperature and the total pressure were fixed. The Mach number was extrapolated at the inlet boundary, and the static pressure was fixed at the outlet boundary. A non-slip and static temperature were imposed on the blade surface. As shown in Figure 1b, the overset grid method was employed to ensure a high computational accuracy. The main grid (black) was a coarse mesh covering the entire computational domain, and the sub grid (red) was a fine mesh used to resolve the flow around a leading edge of the airfoil, where the icing likely occurs. The main and sub grids included 15,961 and 10,251 grid points, respectively, with approximately 26,000 total grid points. Lagrange interpolation was used to exchange data between the main and sub grids. As shown in Figure 1c, the SLDs were released at $7c$ upstream from the blade, where the SLDs were randomly distributed at $\pm 0.1c$ in the y-axis direction. The initial velocity of the SLD was the same as the local velocity of the flow field. In our previous study [18], the predicted ice shape for an ordinary median volume diameter (MVD) of 20 μm was validated by comparing the findings with the experimental data, and a reasonable agreement was observed.

Table 1 summarizes the computational conditions that were set with reference to an experiment performed by Anderson and Tsao [28]. In the simulation, the exposure time was divided into quarters, and steps 2 to 5 of the numerical procedure, as discussed in Section 2, were repeated four times. As summarized in Table 2, four simulation cases were considered to evaluate the influence of each phenomenon on the icing process.

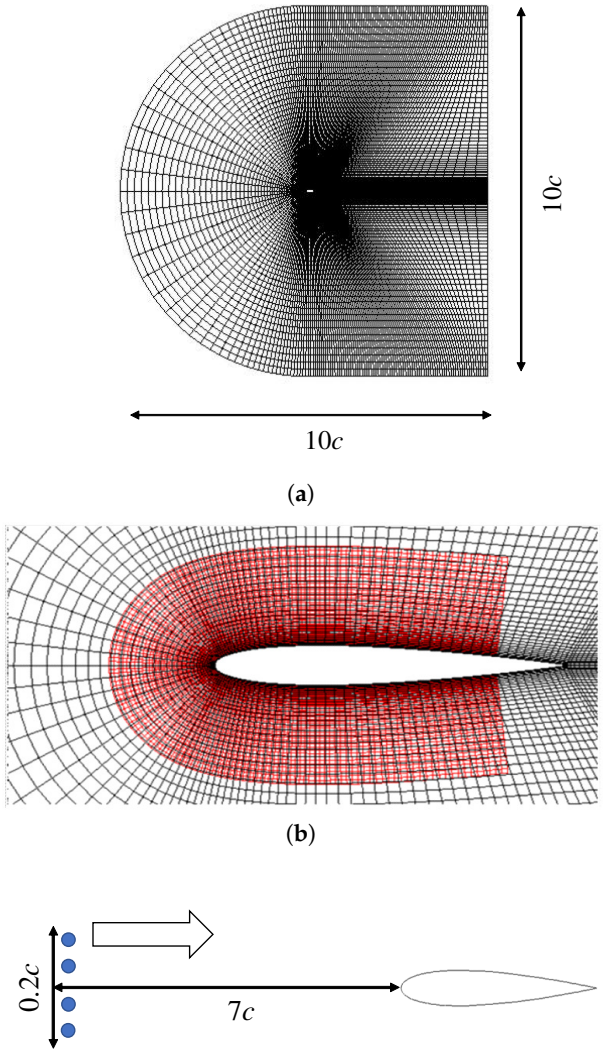


Figure 1. Computational domain and grid for the NACA0012 icing simulation: (**a**) complete domain; (**b**) zoomed-in view around the wing (the main and sub grids are shown in black and red, respectively); (**c**) initial position of droplets.

Table 1. Numerical conditions for the NACA0012 icing simulation.

Parameter	Value
Static temperature	259.15 [K]
LWC	0.73 [g/m^3]
Inflow velocity	77.16 [m/s]
Exposure time	876 [s]
Total number of SLDs for each computational cycle	1,000,000 [-]
Computational cycle number	4 stages
Chord length of airfoil	$c = 0.914$ [m]
Angle of attack of airfoil	$\alpha = 0$ [deg.]
Droplet diameter (Median volume diameter: MVD)	190 [μm]
Droplet density	$\rho_d = 1000$ [kg/m^3]
Droplet temperature	$T_d = 259.15$ [K]
Density of rime ice	$\rho_i = 888$ [kg/m^3]
Density of glaze ice	$\rho_i = 917$ [kg/m^3]
Density of water	$\rho_w = 1000$ [kg/m^3]
Thermal conductivity of ice	$k_i = 2.18$ [W/m·K]
Thermal conductivity of water	$k_w = 0.517$ [W/m·K]
Specific heat of ice	$C_{p,i} = 2050$ [J/kg·K]
Latent heat of water	$LF = 3.344 \times 10^{-3}$ [J/kg]

Table 2. Computational cases for NACA0012 icing simulation.

	Splash-Bounce	Deformation	Breakup
Model 1	w/o	w/o	w/o
Model 2	w	w/o	w/o
Model 3	w	w	w/o
Model 4	w	w/o	w

Figure 2 shows the results for the ice shape and collection efficiency E_{col}. The impinged mass m_{im}, which is defined in Equation (19), is computed using the following equation, with reference to E_{col}:

$$m_{im} = E_{col}\rho_d \frac{4\pi}{3}\left(\frac{1}{2}MVD\right)^3, \tag{21}$$

and this mass is a key factor to determine the ice shape.

Figure 2a presents a comparison of the ice shape, in which the coordinate systems are non-dimensionalized using the chord length of the airfoil, c. The ice shape covers the leading edge of the airfoil. Under real and experimental conditions, however, the ice shape is extremely complex and cannot be easily reproduced using the present simulation. Therefore, instead of reproducing the ice shape, we focus on the icing area because it is a key parameter for the design of anti-icing devices for the airfoil. In Model 2 (i.e., the splash-bounce model), the icing area becomes narrow, and the limitation location of the icing moves toward the leading edge. Figure 2b shows the collection efficiency at the final step of the four steps. The horizontal axis represents the distance from the leading edge of the airfoil non-dimensionalized by c. The positive and negative values of the horizontal axis represent the location of the airfoil on the suction (upper) and pressure (lower) surfaces, respectively. Because the AoA is zero, the collection efficiency is maximized around the leading edge. In Model 2, the region of the non-zero collection efficiency becomes narrow, and it corresponds to the iced area.

Figures 2c,d show the ice shape and collection coefficient pertaining to Model 3 (deformation model). Owing to the insignificant difference between Models 1 and 3, the influence of the deformation can be considered to be extremely small in the icing process.

The effect of the breakup phenomenon is shown in Figures 2e,f. In Model 4 (breakup model), the icing limitation moves toward the leading edge, and the icing decreases. The iced region is in better agreement with the experimentally obtained region compared to that in the other cases. The droplet collection efficiency decreases in the regions farther from the leading edge when considering the

breakup phenomenon. Therefore, the impingement characteristics change owing to the breakup of the droplets, and the icing limit changes with the increase in the intensity of the splash and bounce phenomena. Accordingly, in the SLD simulation, the splash-bounce model and the breakup model yield a reasonable icing area, and the effect of the deformation is minimal.

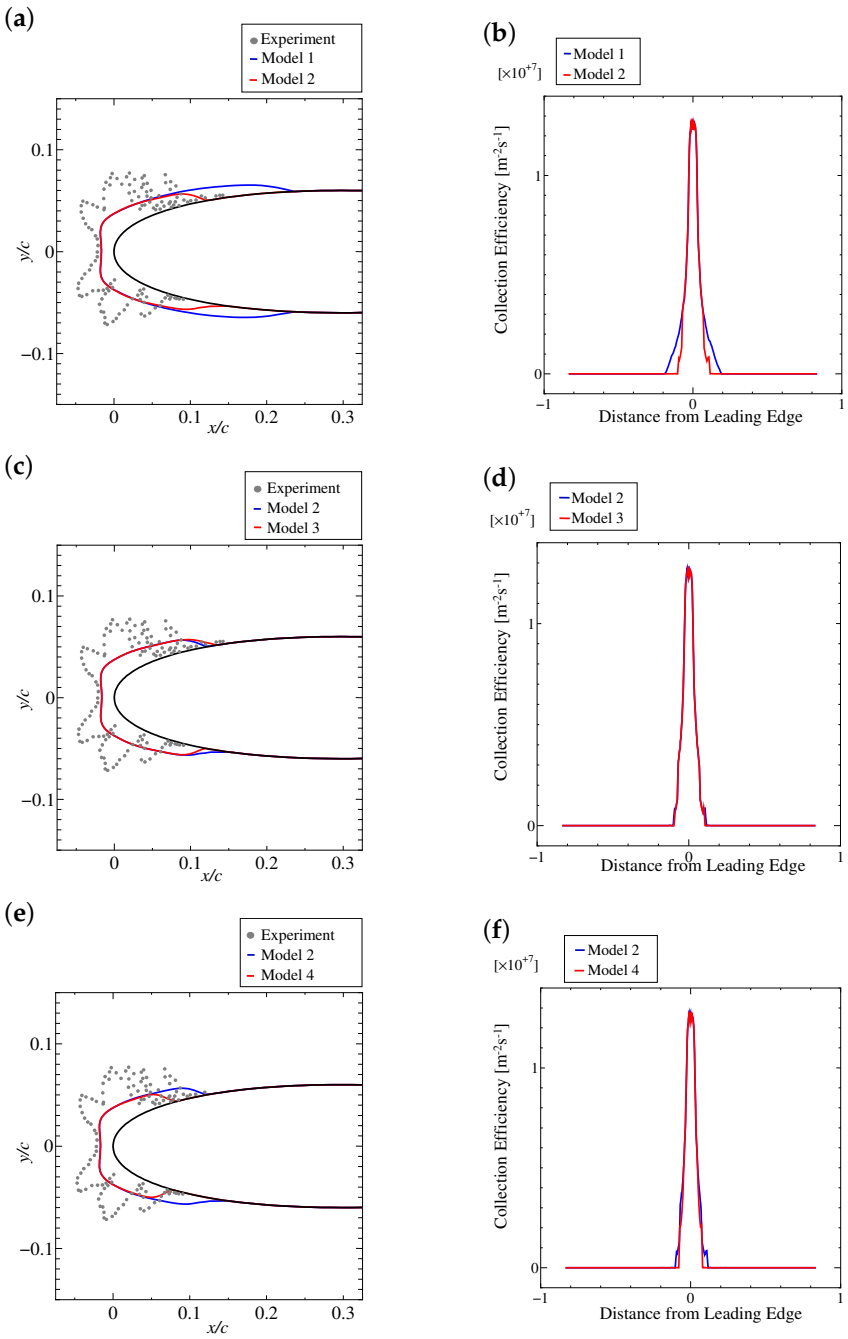


Figure 2. Comparison of ice shapes and collection efficiency for different SLD models: (**a**,**b**), Models 1 and 2; (**c**,**d**), Models 2 and 3; (**e**,**f**), Models 2 and 4.

4. Icing Simulation for Axial Fan

A three-dimensional SLD icing simulation for a commercial axial fan (Kairyu series A2D6H-411, Showa Denki Co., Osaka, Japan) was performed. Although the axial fan has 12 rotor blades, only one blade was examined to simplify the problem. At the inlet boundary, the velocity and total temperature were fixed, and the Mach number was extrapolated. The periodic boundary condition was imposed

in the circumferential direction. At the inlet boundary, the velocity and total temperature were fixed, and the Mach number was extrapolated. At the outlet boundary, the static pressure was fixed. A non-slip and static temperature were imposed on the blade surface. The overset grid method was used to improve the computational accuracy, with the total grid points being approximately 6 million, as shown in Figure 3. The computational conditions are summarized in Table 3. This method has been validated in our previous study [18], in which the icing and shedding for the MVD of 30 µm was examined. The total exposure time was 15 s. Three computational cycles were performed, with the exposure time for one cycle being 5 s.

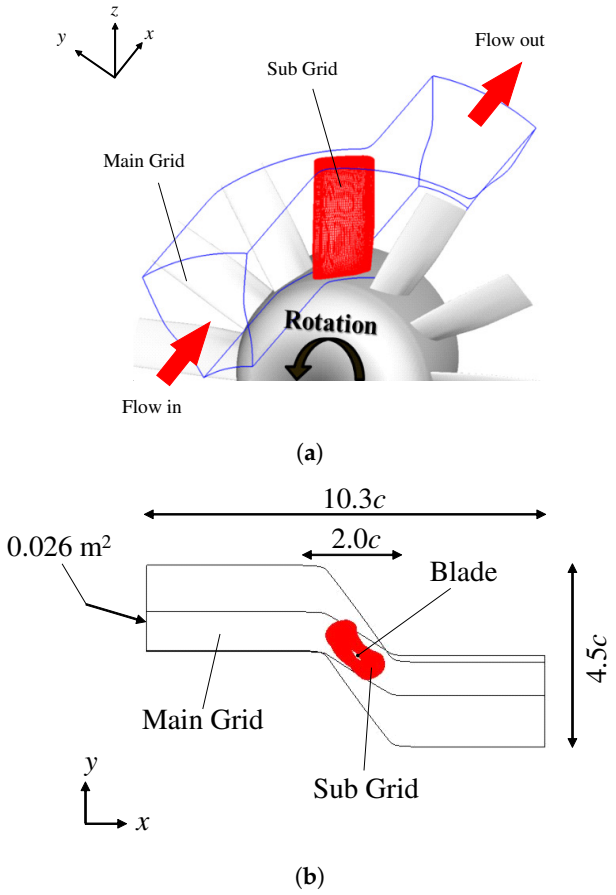


Figure 3. Flow around axial fan and computational domain: the main and sub grids are shown in blue and red, respectively. (**a**) Overview and (**b**) top view of the computational grid.

Table 3. Numerical conditions for the axial fan icing simulation.

Parameter	Value
Static temperature	268.15 [K]
Exposure time	15 [s]
Rotational speed	1800 [rpm]
Mass flow rate	5.2 [kg/s]
Droplet diameter (MVD)	200 [μm]
Total number of SLDs for each computation cycle	1,000,000 [-]
LWC	1.54 [g/m^3]
Inflow velocity	17.2 [m/s]
Chord length of airfoil	$c = 0.073$ [m]
Angle of attack of airfoil	$\alpha = 0$ [deg.]
Density of rime ice	$\rho_i = 888$ [kg/m^3]
Density of glaze ice	$\rho_i = 917$ [kg/m^3]
Density of water	$\rho_w = 1000$ [kg/m^3]
Density of flow	$\rho_f = 1.25$ [kg/m^3]
Thermal conductivity of ice	$k_i = 2.18$ [W/m· K]
Thermal conductivity of water	$k_w = 0.517$ [W/m· K]
Specific heat of ice	$C_{p,i} = 2050$ [J/kg·K]
Specific heat of water	$C_{p,i} = 4218$ [J/kg·K]
Latent heat of water	$LF = 3344 \times 10^{-3}$ [J/kg]

Four different cases, as summarized in Table 4, were examined to verify the effect of the SLD model and the temperature of the droplets on the icing. In general, the surface tension and viscosity of the SLD vary owing to the temperature of the droplet; therefore, the temperature affects not only the icing phenomenon but also the SLD behavior. The decrease in the SLD temperature corresponds to an increase in the surface tension and viscosity, as shown in Equations (6) and (8), respectively.

Table 4. Computational conditions for axial fan icing.

	Splash-Bounce	Deformation	Breakup	SLD Temp. [°C]
Case 1	w/o	w/o	w/o	−5
Case 2	w	w	w	−5
Case 3	w	w/o	w/o	−5
Case 4	w	w/o	w/o	−15

Figure 4 shows the comparison of the effect of the SLD models (splash-bounce, deformation, and breakup) on E_{col} for the blade surface. The leading and trailing edges are represented as "L.E." and "T.E.", respectively. Figures 4a,b show the values of E_{col} on the pressure and suction surfaces in Case 1, in which the SLD model is not considered. The maximum value of E_{col} occurs around the leading edge because the droplet directly impinges and adheres to this area. On the pressure side, the values are distributed on the entire surface, and E_{col} increases at the region close to the hub and trailing edge. On the suction side, E_{col} is extremely small. Figures 4c,d show the E_{col} pertaining to the SLD model of Case 2. The distribution is highly similar to that shown in Figures 4a,b. The values are distributed at the region near not only the hub but also the tip on the pressure side. On the suction side, E_{col} is very small.

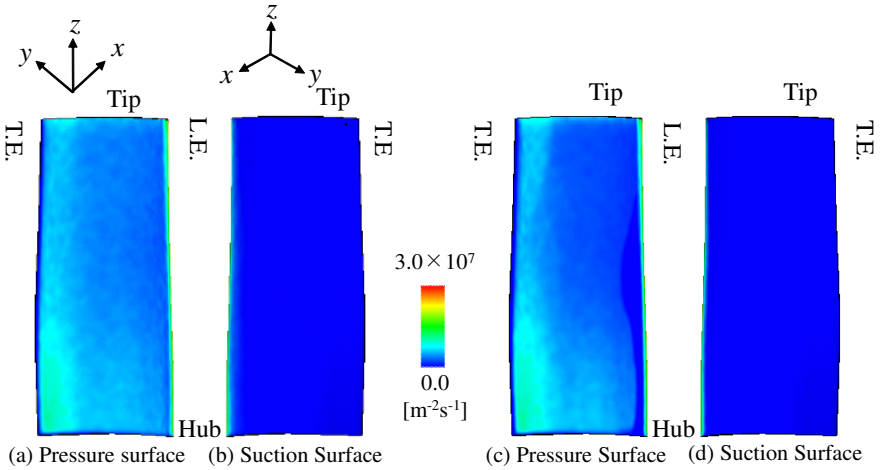


Figure 4. Collection efficiency: (**a**,**b**) w/o SLD model (Case 1) and (**c**,**d**) w/ SLD model (Case 2).

Next, we discuss the influence of the number of SLD in each event listed in Table 5. The ratio of the number of SLDs in each event to the total number of SLDs is defined as

$$R_{event} = \frac{N_{event}}{N_{total}} \times 100[\%]. \tag{22}$$

The number of total SLDs is denoted as N_{total}, and the number of SLDs in each event is denoted as N_{event}; *event* here refers to splash, bounce, and adherence.

Table 5. Effect of the SLD model and temperature on each event.

	R_{adhere} [%]	R_{splash} [%]	R_{bounce} [%]
Case 1	40.3	–	–
Case 2	33.0	24.3	18.4
Case 3	33.0	24.3	18.3
Case 4	35.1	21.5	15.4

In Case 1, the number of adhered particles is 40.3% the total number of SLDs, and only adherence occurs since the splash-bounce model is absent. In contrast, when considering the SLD model, R_{adhere} decreases, whereas R_{splash} and R_{bounce} appear. Moreover, R_{bounce} is smaller than R_{splash}. Therefore, the number of adhered particles decreases by 7.3%. Owing to the similar distributions in Cases 2 and 3, the difference in the collection efficiency distribution, as shown in Figure 4, pertains to the consideration of the splash-bounce model. Moreover, the number of deformed and broken particles is negligibly small. These results indicate that, although the influence of the deformation and breakup events is extremely small, the splash-bounce phenomenon considered influences the icing process. In Case 4, the droplet temperature decreases, and R_{adhere} increases; however, R_{splash} and R_{bounce} decrease owing to the change in the physical properties. Therefore, we further examined the icing phenomenon considering the splash-bounce model without the deformation and breakup models (Cases 1, 3, and 4).

Figure 5 shows the ice thickness on the pressure surface for each case. As discussed, the icing tends to occur in the pressure surface and not on the suction surface. The maximum ice thickness occurs at the leading edge (approximately 1.2 mm in Cases 1 and 3 and 1.5 mm in Case 4). In Case 1, as shown in Figure 5a, the icing covers the complete surface owing to the absence of the splash-bounce model. In Case 3, the ice thickness is smaller than that in Case 1 in the region close to the leading edge, and the thickness increases closer to the trailing edge owing to the bouncing of the SLD at the leading edge. This phenomenon is especially notable in Case 4.

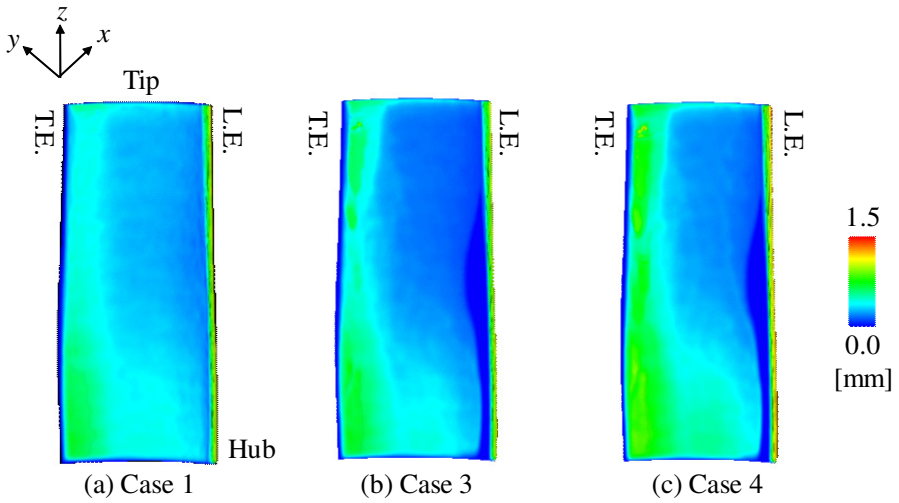


Figure 5. Ice thickness distribution on the pressure surface: (**a**) Case 1, (**b**) Case 3, and (**c**) Case 4.

Figure 6a shows the flow field in terms of the Mach number at 90% span of the blade without the icing (i.e., before icing) for Case 3. In the suction side, flow separation occurs in the region close to the trailing edge. Figure 6b shows the flow field after the icing, that is, corresponding to the icing distribution at 15.0 s. The iced region (shown in black) appears around the leading and trailing edges on the pressure surface. The flow separation region expands owing to the icing.

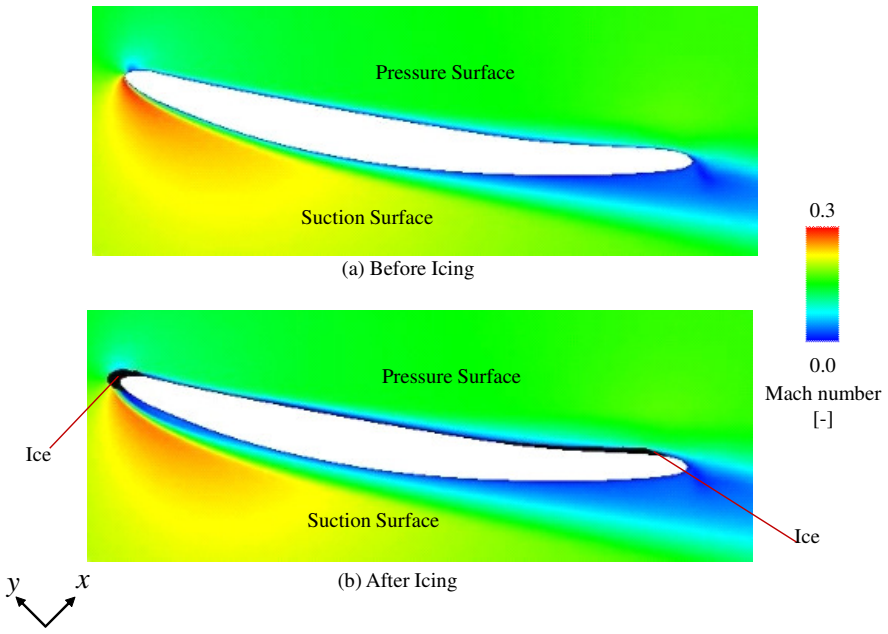


Figure 6. Mach number distribution at 90% span of the fan for Case 3.

Moreover, we discuss the time variation of the loss of the mass flow rate. The reduction rate of flow R_Q is defined in terms of the flow rate Q, as

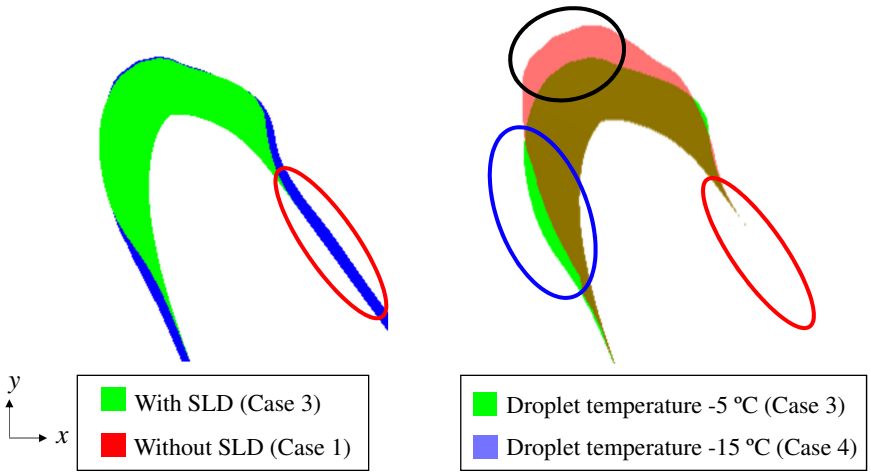
$$R_Q[\%] = \frac{Q_{after} - Q_{before}}{Q_{before}} \times 100. \tag{23}$$

Here, Q_{before} and Q_{after} denote the mass flow rate before and after icing, respectively. Q is defined as

$$Q = \int_S \rho_f \boldsymbol{u}_f \cdot d\boldsymbol{s}, \tag{24}$$

where $S(= 0.026\,\mathrm{m}^2)$ is the cross-sectional area of the flow passage, $d\boldsymbol{s}$ is the surface area vector, and ρ_f is the local density of the fluid. As time advances, the ice grows, and it disturbs and blocks the flow. Therefore, R_Q increases with time; specifically, R_Q = 2.0%, 2.9%, 4.3%, and 6.9% at 15 s, 30 s, 45 s, and 60 s, respectively. If the exposure time is sufficiently large, there is considerable ice growth, and it may be peeled off from the blade. Such ice shedding can critically damage the engine material and components. However, in this study, the exposure time was too small to reproduce the ice shedding owing to the limitations of the computational cost. This phenomenon must be addressed in future research.

Figure 7 shows the ice shape around the leading edge at the midspan of the blade. Figure 7a presents a comparison of the effects of the SLD model on the ice shape, i.e., Cases 1 and 3. The icing occurs at the leading edge in Case 3, whereas the icing region expands in Case 1, as indicated by the red circle. These findings are in agreement with the ice thickness distribution, as shown in Figures 5a,b. Figure 7b shows the effect of the SLD temperature on the ice shape, i.e., Cases 3 and 4. In Case 3, the icing occurs at not only the leading edge (circled in black) but also the suction ($-x$) side. The ice on the suction side close to the leading edge is the glaze ice generated by the water-runback (circled in blue), which occurs because the SLD temperature is relatively higher than that in Case 4. In Case 4, the ice at the leading edge thickens (circled in black) owing to the presence of rime ice; specifically, the SLD instantaneously freezes when the droplet collides on the surface. This phenomenon occurs because the water-runback and splash-bounce phenomena do not occur. In addition, the icing on the pressure side does not occur in both the cases, as shown by the red circle.



(a) Comparison between case 1 and 3 (b) Comparison between case 3 and 4

Figure 7. Ice shape around the leading edge at the midspan.

5. Conclusions

Icing simulations were performed considering the specific phenomena of SLDs i.e., splash, bounce, deformation, and breakup.

The results of the SLD simulation for NACA0012 were in reasonable agreement with the experimental data in terms of the ice shape. The effect of the computational models of the SLD-specific phenomena on the icing was clarified. Specifically, the splash and bounce events considerably influence the icing phenomena, whereas the effects of deformation are negligibly small.

In the SLD icing simulation considering the axial fan, when the SLD-specific phenomena were taken into account, the collection efficiency was observed to be distributed at the region near not only the hub but also the tip on the pressure side. The SLD icing thus affected the flow field around the fan blade, and flow separation was observed behind the icing layer. Moreover, the ice thickness around the leading edge when the SLD-phenomena was considered was smaller than that when not considering

the SLD phenomena, and the ice thickness was noted to increase toward the trailing edge. With the decrease in the droplet temperature, the number of droplets adhering on the blade increased, and the number of droplets that splashed and bounced decreased.

Author Contributions: Conceptualization, T.T. and M.Y.; methodology, T.T. and M.Y.; validation, T.T., K.F., H.M. and M.Y.; formal analysis, T.T.; investigation, T.T., K.F., H.M. and M.Y.; writing—original draft preparation, T.T.; writing—review and editing, K.F., H.M., N.F. and M.Y.; visualization, T.T.; supervision, M.Y.; project administration, M.Y.; funding acquisition, M.Y. All authors have read and agreed to the published version of the manuscript.

Funding: This research was partially supported by the Ministry of Education, Culture, Sports, Science and Technology through a Grant-in-Aid for Scientific Research (B) (Grant No. 16H03918).

Acknowledgments: The authors are grateful to Miki Shimura, former graduate school student of the Tokyo University of Science, for her pioneering research.

Conflicts of Interest: The authors declare no conflict of interest.

Abbreviations

The following abbreviations are used in this manuscript:

LWC	Liquid water content
MVD	Median volume diameter
SLD	Super-cooled large droplet

References

1. Zhang, X.; Min, J.; Wu, X. Model for aircraft icing with consideration of property-variable rime ice. *Int. J. Heat Mass Transf.* **2016**, *97*, 185–190.
2. Fortin, G.; Ilinca, A.; Laforte, J.L.; Brandi, V. A new roughness computation method and geometric accretion model for airfoil icing. *J. Aircr.* **2004**, *41*, 119–127.
3. Janjua, Z.A.; Turnbull, B.; Hibberd, S.; Choi, K.S. Mixed ice accretion on aircraft wings. *Phys. Fluids* **2018**, *30*, 027101.
4. Szilder, K.; Lozowski, E.P. *Progress Towards a 3D Numerical Simulation of Ice Accretion on a Swept Wing Using the Morphogenetic Approach*; SAE Technical Paper, No. 2015-01-2162; SAE: Warrendale, PA, USA, 2015.
5. Szilder, K.; Yuan, W. In-flight icing on unmanned aerial vehicle and its aerodynamic penalties. *Prog. Flight Phys.* **2017**, *9*, 173–188.
6. Shen, X.; Lin, G.; Yu, J.; Du, C. Three-dimensional numerical simulation of ice accretion at the engine inlet. *J. Aircr.* **2013**, *50*, 635–642.
7. Wang, Z.; Zhu, C. Study of the effect of centrifugal force on rotor blade icing process. *Int. J. Aerosp. Eng.* **2017**, *2017*, 8695170.
8. Narducci, R.; Kreeger, R.E. *Analysis of a Hovering Rotor in Icing Conditions*; NASA-TM217126; NASA: Washington, DC, USA, 2012.
9. Mingione, G.; Brandi, V. Ice accretion prediction on multielement airfoils. *J. Aircr.* **1998**, *35*, 240–246.
10. Wright, W.B.; Potapczuk, M.G. Computational simulation for large droplet icing. In Proceedings of the FAA International Conference on Aircraft Inflight Icing, Springfield, VA, USA, 6–8 May 1996; Report No. DOT/FAA/AR-96/81; Volume II, pp. 545–555.
11. Zhang, C.; Liu, H. Effect of drop size on the impact thermodynamics for supercooled large droplet in aircraft icing. *Phys. Fluids* **2016**, *28*, 062107.
12. Wang, C.; Chang, S.; Hongwei, W. Lagrangian approach for simulating supercooled large droplets' impingement effect. *J. Aircr.* **2015**, *52*, 524–537.
13. Wang, C.; Chang, S.; Leng, M.; Yang, B. A two-dimensional splashing model for investigating impingement characteristics of supercooled large droplets. *Int. J. Multiph. Flow* **2016**, *80*, 131–149.
14. Honsek, R.; Habashi, W.G.; Aube, M.S. Eulerian modeling of in-flight icing due to supercooled large droplets. *J. Aircr.* **2008**, *45*, 1290–1296.
15. Bilodeau, D.R. Eulerian modeling of supercooled large droplet splashing and bouncing. *J. Aircr.* **2015**, *52*, 1611–1624.

16. Raj, L.P.; Lee, J.W.; Myong, R.S. Ice accretion and aerodynamic effects on a multi-element airfoil under SLD icing conditions. *Aerosp. Sci. Technol.* **2019**, *85*, 320–333.
17. Cao, Y.; Xin, M. Numerical simulation of supercooled large droplet icing phenomenon: A Review. *Arch. Comput. Methods Eng.* **2019**, doi:10.1007/s11831-019-09349-5.
18. Hayashi, R.; Yamamoto, M. Numerical Simulation on Ice Shedding Phenomena in Turbomachinery. *J. Energy Power Eng.* **2015**, *9*, 45–53.
19. Yee, H.C. *Upwind and Symmetric Shock-Capturing Schemes*; NASA-TM-89464; NASA: Washington, DC, USA, 1987.
20. Fujii, K.; Obayashi, S. *Practical Applications of New LU-ADI Scheme for the Three-Dimensional Navier–Stokes Computation of Transonic Viscous Flows*; AIAA Paper 86-0513; AIAA: Reston, VA, USA, 1986.
21. Kato, M.; Launder, B.E. The modeling of turbulent flow around stationary and vibrating square cylinders. In Proceedings of the 9th Symposium on Turbulent Shear Flows, Kyoto, Japan, 16–18 August 1993; Volume 1, pp. 10–14.
22. Clift, R.; Grace, J.R.; Weber, M.E. *Bubbles, Drops and Particles*; Academic Press: Cambridge, MA, USA, 1978.
23. Luxford, G. Experimental and Modelling Investigation of the Deformation, Drag and Break-Up of Drizzle Droplets Subjected to Strong Aerodynamics Forces in Relation to SLD Aircraft Icing. Ph.D. Thesis, Cranfield University School of Engineering, Bedford, UK, 2005.
24. Hsiang, L.P.; Faeth, G. Secondary drop breakup in the deformation regime. In Proceedings of the 30th AIAA Aerospace Sciences Meeting and Exhibit, Reno, NV, USA, 6–9 January 1992; p. 110.
25. Wright, W.B. *Further Refinement of the LEWICE SLD Model*; NASA TM-214132; NASA: Washington, DC, USA, 2006; 29p.
26. Wright, W.B.; Potapczuk, M.; Levinson, L. *Comparison of LEWICE and GlennICE in the SLD Regime*; NASA TM-215174; NASA: Washington, DC, USA, 2008; 31p.
27. Özgen, S.; Canibek, M. Ice accretion simulation on multi-element airfoils using extended Messinger model. *J. Heat Mass Transf.* **2009**, *45*, 305.
28. Anderson, D.N.; Tsao, J.C. *Ice Shape Scaling for Aircraft in SLD Conditions*; NASA CR-215302; NASA: Washington, DC, USA, 2008.



© 2020 by the authors. Licensee MDPI, Basel, Switzerland. This article is an open access article distributed under the terms and conditions of the Creative Commons Attribution (CC BY) license (http://creativecommons.org/licenses/by/4.0/).